Characterization of behaviour and hazards of fire and deflagration for high-energy Li-ion cells by over-heating

Ping Ping [a,b], Depeng Kong [c], Jiaqing Zhang [d], Ruoxi Wen [c] and Jennifer Wen [b,*]

[a] *College of Chemical Engineering, University of Petroleum of China, Qingdao 266580, PR China*

[b] *Warwick FIRE, School of Engineering, University of Warwick, Library Road, Coventry CV4 7AL,UK*

[c] *Center for Offshore Engineering and Safety Technology, China University of Petroleum*

[d] *State Grid Anhui Electric Power Research Institute, Hefei, Anhui, 230 022, China*

[*] Correspondence: Jennifer.wen@warwick.ac.uk

Highlights

- Critical incident heat flux that activates deflagration or/and fire is found.
- Duration, evolution and key parameters of fire and deflagration are characterized.
- Underlying reactions for fire and deflagration occurrence are determined.
- Hazards like extreme temperatures of cell and flame, and ejected gas are quantified.
- Revised oxygen consumption method is developed and the heat release is specified.

Abstract:

Fire and deflagration are extreme manifestation of thermal runaway (TR) of Li-ion cells, and they are characterized for fully charged $LiNiCoAlO_2$ (LNCA) 18650 cells in this investigation. The cells are over-heated using a cone calorimeter under different incident heat fluxes. When the cells are exposed to the incident heat flux larger than 35 kW m^{-2}, both fire and deflagration present. The pressure valve opens when the temperature of the cell is higher

than 132 ^{o}C. The fire occurs with the valve opening when the concentration of the venting vapour in the air is higher than the lower flammability limit. The deflagration happens after the cell temperature arrives about 200^{o}C, and is mainly arising from the cathode decomposition, the combustion of solvents and the anode relevant thermal reactions. The extreme temperatures of the cell and the flame during deflagration are over than 820 and 1035 ^{o}C, respectively. The production of CO_x, mass loss, heat release rate (HRR) are quantitative identified, and are found increase as the increasing incident heat flux. Based on revised oxygen consumption method, the HRR and liberated heat during the fire and deflagration for the cells are up to 11.8±0.05 kW and 163.1±1.5kJ, respectively.

Keywords: $LiNiCoAlO_2$ cell; Fire behaviour; Deflagration; Thermal hazard; over-heating

1. Introduction

State-of-the-art commercial Li-ion batteries (LIBs), which possess high energy density, good cycling stability and long lifetime, currently dominant the power sources for portable electronics and are increasingly used in electric vehicles (EV) and grids storage. On the other hand, as revealed by many investigators [1-3], thermal runaway (TR) and its propagation in LIB modules and packs may result in fire and/or explosions under abnormal operations, such as overheating, overcharging, short circuit, puncture, compression or crashing. To enhance the safety of LIBs, numerous efforts have been devoted to developing new cell materials, chemistry, novel cell design and improved battery thermal management systems (BTMS) [4-7]. Although various progress has been achieved, incidents and recalls related to LIBs have still occurred in the consumer market for mobile phones, laptops and EVs as well as airplanes [8, 9]. To meet the ever increasing requirements for high energy and power density LIBs, some relatively new chemistry systems with high energy density have entered the commercial

market. However, the potential risk and associated hazards are not well understood or quantified.

$LiNiCoAlO_2$ (LNCA) is a type of relatively new cathode material which has already been commercially used in LIBs in recent years. Comparing with traditional $LiCoO_2$, $LiMn_2O_4$, $LiFePO_4$ and other cathode materials, LNCA has higher specific capacity, which makes LNCA based cells attractive to the EV application. However, the thermal stability issue of LNCA cells at high temperature is still a problem which hinders its wide application [10]. In order to gain insight of TR and its propagation of LNCA cells, some investigators have conducted failure tests to analyse the behaviour of LNCA cells during TR. Golubkov et al. [11] studied the parameters of TR for two types of 18650 cells (LNCA cells and $LiFePO_4$ cells) using thermal ramp tests to measure the onset and maximum temperature, the composition and quantity of the vent gas. They also examined the dependence of the TR behaviour on the state of charge (SOC). Duh et al. [12] performed TR tests of LNCA cells with 100% SOC. They measured the TR parameters and calculated the enthalpy change liberated by TR of the cells based on adiabatic temperature rise. The averaged enthalpy change during TR was found to be (30.9±4.6) kJ for 18650 LNCA cells. Lammer et al. [13] proposed holistic analysis of thermally induced TR of 18650 LNCA cells. The heat emissions and maximum total gas emission of TR were found to be 31 kJ and 5459 cm^3, respectively. The above studies provided details about TR behaviour and key indicating parameters, and potential mechanisms associated with the thermal stability deterioration of LNCA cells. However, to the best of our knowledge, the fire and deflagration behaviour of LNCA cells have not been quantitatively investigated. When fire or deflagration occurs in LNCA cells, more heat could be released than that when there is only venting without ignition. The energy liberated during TR are typically determined by two methods: (1) multiplying the temperature rise with the heat capacity and the mass for the cell body, or/and gaseous species or/and the sealed canister.

The energy during TR is determined by the contribution from heat change of cell body, or/and gaseous species or/and the sealed canister [12, 14-16]; and (2) the estimated heat of combustion of the flammable LIB composites such as electrolyte, separator, binder and packaging [17, 18]. Neither method takes into account the subsequent effect of potential deflagration, which can result in rapid temperature rise and huge energy release with a short time.

Fire or deflagration resulting from LIB TR and TR propagation poses serious potential hazards. Key characteristics which should be investigated include the duration of fire and/or deflagration, the evolution of the TR and its propagation, the critical parameters at the onset of fire and deflagration, the time to ignition and the critical incident heat flux that activate fire and deflagration. The resulting hazards including extreme temperatures of both the cell and the flame, heat released by the fire and/or deflagration and the ejected gases need to be quantified as such information is not only important to aid the design of robust and reliable battery module and BTMS but also crucial for effective fire protection and emergency response and evacuation.

In the present study, laboratory tests have been conducted by subjecting LNCA cells to radiant panels. The results have been analysed to derive the critical condition for TR and the evolution from venting to fire and deflagration. Measurements have been conducted for the cell surface temperature, flame temperature, heat release rate, time to ignition, duration of ignition, mass loss and production of CO_x. The energy source and energy loss of the cells during the tests are analysed. Recommendations have been formulated for thermal management and fire protection.

2. Experimental Setup

The test rig: The schematic of the test rig is shown in Fig. 1. A radiant heater of cone calorimeter was placed above the cell to imitate different heating conditions. Two K-type

(chromel–alumel) thermocouples (0.5 mm diameter) with a response time of 1 s and accuracy of ±1.5°C were either sticking around the testing cell or hanging on the upside of the cell to obtain the surface temperature of the cell and the flame temperature while fire jetting. Since the cathode material of the experiment is unstable under high temperature, to prevent the test system from being damaged during the experiment, the protection screen of the cone calorimeter was put down to prevent the exploding electrolyte injection and jet fire from widely spreading and fire jetting. The combustion products such as toxic gases were collected by the cone calorimeter and were transported away through a ventilation system. To prevent the system from being damaged by the injected electrolyte and jet fire, the cell was placed up on a flame–protection shield with holder. A weighing sensor was placed underneath the flame-protection shield to simultaneously measure the mass loss of the testing cell. A digital camera which was protected by the protection screen of the cone calorimeter was used to record the burning behaviour and jetting process of the tested cell. The exhaust hood was set to collect the combustion products mixed with ambient air and an oxygen analyzer was used to measure the oxygen depletion during the test. The heat release rate can be measured based on the combustion products and oxygen depletion. Each test was ended after the flame was extinguished without any suspicious phenomenon. All tests were repeated three times to reduce the test errors.

Cell fabrication and cycling: The cells (Panasonic) are 18650 cylinders with dimension of 18 mm in diameter and 65.2 mm in height. Their typical capacity is 3.2 Ah and the total mass is about 48.5±0.05g. Cells were pre-cycled using a cycler (Neware) at 0.1 C current rate within 2.5~4.2 V for three cycles and then followed by a constant voltage charging at 4.2 V, to achieve 100% SOC. In order to ensure the accuracy of the SOC, the charge and discharge cycling was completed within 10h before the fire test.

The plastic packaging of all the testing cells were stripped before experiment to

eliminate the influence of thermal decomposition of the packaging.

Thermal analysis and structure characterization of cell materials: After the cell was dissembled, the electrolyte was collected, the separator and the electrode were picked out and washed with DMC. The washed separator and electrode were then dried in the vacuum oven overnight under 40ºC. Thermal stabilities of the cell materials were studied by differential scanning calorimetry (DSC, Mettler Toledo). Separator, electrode and electrolyte with specific mass were added and sealed in the DSC crucible. The whole process was performed in the argon filled glove box. The sampling robot pierced the lid of hermetically sealed crucible immediately before the test. The DSC test was run in a nitrogen filled environment to prevent the samples from contacting with air. A heating rate of 10 ºC/min from 50 ºC to 500 ºC was used for the test. The heat flow was calculated based on the weight of the entire sample. X-ray powder diffraction (XRD) was carried out using a Bruker Analytical X-ray System with Cu Kα radiation source filtered by a thin nickel plate.

3. Methodology

To interpret the complex progression of a cell from being over-heated to TR, and eventually to occurrence of fire or deflagration, mathematical model is built in this study. The model considers the intricate energy transport within and outside of the cell, including thermal radiation from the heater and possible fire or deflagration outside of the cell, the thermal reactions taking place in the cell, the effect of the venting vapour and ejecta, the thermal energy transformed from the electrical energy stored in the cell, and the heat dissipation arising from heat transfer to the atmosphere caused by convection and radiation.

During the over-heating tests, the cells were exposed to the radiating heat panel. Once the fire or deflagration occurs, the cells were also exposed to the thermal radiation of the flame. Therefore, the external heat source of the tested cells constitute from the radiation from the heater and the flame, which can be characterized as:

$$Q_{ext} = Q_{rad,heater} + Q_{rad,flame} = 1000S[\alpha_{eff} Q_{heater} + VQ_{E,flame}\tau] \quad (1)$$

Where, 1000 converts figures in kW to W; S is the surface area, m^2; α_{eff} is the average effective absorptivity; Q_{heater} is the incident heat flux of the heater, kw m^{-2}; V is the view factor; $Q_{E,flame}$ is the flame emissive power, kw m^{-2}; and τ is the atmospheric transmissivity. Details of how to determine these parameters can be found in Ref. [19].

Under elevated temperature, cell materials react with each other and release enormous heat and gas. The heat generated by the electrodes, electrolyte, separator, and other components of a cell boosts exponentially, which is always described by the Arrhenius equation:

$$Q_{reac} = \sum H_i m_i A_i \exp(-\frac{E_{a,i}}{RT}) f(\alpha_i) \quad (2)$$

Where, H_i is the enthalpy of one of the specific thermal reactions that among cell materials, J g^{-1}; m_i is the mass for the specific thermal reactions, g; A_i, is the frequency factor, s^{-1}; $E_{a,i}$ is the activation energy, J mol^{-1}; R is the gas constant, 8.314 J $K^{-1}mol^{-1}$; α_i is the fractional degree of conversion and $f(\alpha_i)$ is the reaction model.

Moreover, part of the electrical energy stored in the cell always converts into thermal energy during the process of TR. The ratio of how much electrical energy converts to heat, is related with the thermal behaviour of the cell. With the development of the separator melting process, the contact surface between the cathode and anode increases, which leads to the Joule heat generated by the short circuit also increase. To determine the quantity of electrical energy that released as heat, an energy conversion efficiency factor η_{eff} is employed. Specifically, according to different melting stages of separator, various efficiency factors are defined as $\eta_{eff,i}$. Then the electrical energy that released as heat is given by:

$$Q_{elec} = \eta_{eff,i} Q_{elec,act} = \eta_{eff,i} \int IUdt \quad (3)$$

Where, Q_{elec} is the actual electrical energy stored in the tested cells, W; According to the melting stages of separator and to fit the tests, $\eta_{eff,1} \approx 0.1$, $\eta_{eff,2} \approx 0.2$, $\eta_{eff,3} \approx 0.7$ were used; I is the

current, A; U is the voltage, V; and t is the time, s.

From the next section, it can be found that the opening of the pressure valve was followed by vapour venting and ejecta which accompanied the fire or deflagration. The influence of venting and ejecta, hence, need to be incorporated in the energy balance of the cell. To classify the ratio of the energy leaving with venting and ejecta, an ejection efficiency factor ξ_{eff} (ξ_{eff} =0.23, as reported in Ref. [20]) is used following [20]:

$$Q_{eject} = \xi_{eff,i} m_{eject,i} C_{p,j} (T_{eject,i} - T_{am}) \quad (4)$$

Where, Q_{eject} is the energy brought out from the cell by the vapour and ejecta, W; $m_{eject,i}$ and $T_{eject,i}$ are the mass and temperature of the vapour or ejecta, respectively, g and K; C_p is the specific heat of the jelly roll of the cell, J kg^{-1} K^{-1}; T_{am} is the temperature of the ambient, K.

The heat loss of the cell not only include the heat taken away by the vapour and ejecta, but also consists of:

$$Q_{conv} + Q_{rad,cell} = S[h_{conv}(T_{cell} - T_{am}) + \varepsilon_{eff}\sigma(T_{cell}{}^4 - T_{am}{}^4)] \quad (5)$$

Where, Q_{conv} is heat source of the convection, W; h_{conv} is convective heat transfer coefficient, W m^{-2} K^{-1}; ε_{eff} is the average effective emissivity and equals to 0.32 [21]; and σ is the Stefan–Boltzmann constant.

Then the energy balance equation of the cell is given by:

$$\rho C_p \frac{\partial T}{\partial t} = \frac{1}{r}\frac{\partial}{\partial r}(\lambda r \frac{\partial T}{\partial r}) + \frac{1}{r^2}\frac{\partial}{\partial \varphi}(\lambda \frac{\partial T}{\partial \varphi}) + \frac{\partial}{\partial z}(\lambda \frac{\partial T}{\partial z}) + Q_{ext} + Q_{rec} + Q_{elec} - Q_{ejcect} - Q_{conv} - Q_{rad,cell} \quad (6)$$

Where, ρ is the density, kg m^{-3}; C_p is the specific heat capacity of the cell, J kg^{-1} K^{-1}; λ is the thermal conductivity, W m^{-1} K^{-1}.

Besides the energy balance of the cell, the energy released by the fire or deflagration of the cell is critical for fire control and determination of the firefighting system. In order to characterize the heat released by the fire or deflagration, the heat release rate (HRR) is calculated. HRR is the driving force that influences many other parameters associated with the

fire condition and can be obtained by using the oxygen consumption principle (OCP). The OCP is based on the Thornton's rule [22], which is, for a large number of organic liquids or gases, an approximately constant net amount of heat is released per unit mass of O_2 consumed for complete combustion. This constant is found as 13.1 MJ kg^{-1} by Huggett et al. [23] and is accurate with very few exceptions to within ±5% [24]. In fact, combustion is often incomplete in fire accidents resulting in the formation of carbon monoxide. Hence, the HRR can be determined from oxygen consumption, carbon dioxide and carbon monoxide generation measurements.

If we assume N_2, O_2, CO_2 and H_2O primarily make up the air entering the testing system, and over 99% of the exhaust gas flow is composed of N_2, O_2, CO_2 CO and H_2O, then the mass flow rate of the incoming air and the exhaust gas flow is determined as:

$$\dot{m}_{in} = \sum \dot{m}_i^0 \qquad \dot{m}_{ex} = \sum \dot{m}_i \tag{7}$$

Where, $\dot{m}_{in}$ and $\dot{m}_{ex}$ are the mass flow rate of the incoming air and the exhaust gas flow, respectively, kg s^{-1}; $\dot{m}_i^0$ is the mass flow rate of specie N_2, O_2, CO_2 or H_2O in the incoming air, kg s^{-1}; $\dot{m}_i$ is the mass flow rate of specie N_2, O_2, CO_2, H_2O or CO in the exhaust duct, kg s^{-1}.

The HRR of the combustion process is obtained by using OCP:

$$\dot{Q} = E(\dot{m}_{O_2}^0 - \dot{m}_{O_2}) - (E_{CO} - E)(\Delta\dot{m}_{O_2})_{CO} \tag{8}$$

Where, $\dot{Q}$ is the HRR, kW; E is the heat release per unit mass of O_2 consumed, 13.1 MJ kg^{-1}; E_{CO} is the heat release per unit mass of O_2 for CO, 17.6 MJ kg^{-1} and $(\Delta\dot{m}_{O_2})_{CO}$ is the assumed mass flow rate of O_2 consumed for the conversion of CO to CO_2, kg s^{-1}.

To calculate $\dot{Q}$, the mass flow rates $\dot{m}_{O_2}^0$, $\dot{m}_{O_2}$ and $(\Delta\dot{m}_{O_2})_{CO}$ need to be specified. For the detailed calculation process, interested readers may refer to Ref. [24], the following part

summaries the key equations to perform the calculation. Since the test system is open, the mass flow rate of the exhaust gases in the duct rather than the incoming air is available:

$$\dot{m}_{ex} = 26.54 \frac{A k_c}{f(\mathrm{Re})} \sqrt{\frac{\Delta p}{T_{ex}}} \tag{9}$$

Where, A is cross-sectional area of the duct, m^2; k_c is velocity profile shape factor; Δp is pressure drop across the orifice plate, Pa; T_{ex} is exhaust gas temperature at the orifice plate, K.

To find a relation between $\dot{m}_{ex}$ and $\dot{m}_{in}$, the oxygen depletion factor is defined as:

$$\phi = \frac{\dot{m}^0_{O_2} - \dot{m}_{O_2}}{\dot{m}^0_{O_2}} = \frac{X^0_{O_2}(1 - X_{CO_2} - X_{CO}) - X_{O_2}(1 - X^0_{CO_2})}{(1 - X_{O_2} - X_{CO_2} - X_{CO}) X^0_{O_2}} \tag{10}$$

Where, $X^0_{O_2}$ and $X^0_{CO_2}$ are the measured mole fraction of O_2 and CO_2 in the incoming air, respectively; X_{O_2}, X_{CO_2} and X_{CO} are the measured mole fraction of O_2, CO_2 and CO in the exhaust gases, respectively.

Given N_2 is almost conserved in the tests, then by combining $\dot{m}_{N_2} = \dot{m}^0_{N_2}$ with Eq. (6), the following equation can be obtained:

$$\frac{\dot{m}_{in}}{M_{in}} = \frac{(1 - X_{H_2O})(1 - X_{O_2} - X_{CO_2} - X_{CO})}{(1 - X^0_{H_2O})(1 - X^0_{O_2} - X^0_{CO_2})} \frac{\dot{m}_{ex}}{M_{ex}} \tag{11}$$

Where, M_{in} and M_{ex} are the molecular weight of incoming air and exhaust gases, respectively, kg s^{-1}; $X^0_{H_2O}$ and X_{H_2O} are the mole fraction of water vapour in the incoming air and exhaust gases, respectively.

The assumed mass flow rate of O_2 consumed for the conversion of CO to CO_2 is given by:

$$(\Delta \dot{m}_{O_2})_{CO} = \frac{1}{2} \dot{m}_{CO} \frac{M_{O_2}}{M_{CO}} = \frac{1}{2} \dot{m}_{O_2} \frac{X_{CO}}{X_{O_2}} = \frac{1 - \phi}{2} \frac{X_{CO}}{X_{O_2}} \frac{M_{O_2}}{M_{in}} X^0_{O_2} \tag{12}$$

Based on the above equations, Eq. (7) then can be converted to:

$$\dot{Q} = \left[E\phi - (E_{CO} - E)\frac{1-\phi}{2}\frac{X_{CO}}{X_{O_2}} \right] M_{O_2}(1 - X^0_{H_2O}) X^0_{O_2} \frac{\dot{m}_{in}}{M_{in}} \quad (13)$$

Confirmed by our analysis in section 4.3 and previous search [25, 26], O_2 is generated by the decomposition of cathode at elevated temperatures. This special character of Li-ion cells remind us the calculation of HRR based on OCP need to be revised. Considering the O_2 released from cathode decreases the value of $(\dot{m}^0_{O_2} - \dot{m}_{O_2})$ described in Eq.(8), the heat generated by this part of O_2 need to be added to the value of $\dot{Q}$ obtained from Eq.(13). From our investigation in section 4.3, the LNCA cathode might completely or partly decompose to Ni or NiO whilst release O_2. From the safety perspective, in this study, the O_2 generated by the cathode is supposed to be the maximum value, which means the whole O in the cathode structure is released for conservative calculation. Then the quantity of O_2 generated from the cathode, which is defined as $(\Delta\dot{m}_{O_2})_{NCA}$, is dependent on the mass of the cathode.

Therefore, Eq. (12) can be revised to:

$$\dot{Q} = \left[E\phi - (E_{CO} - E)\frac{1-\phi}{2}\frac{X_{CO}}{X_{O_2}} \right] M_{O_2}(1 - X^0_{H_2O}) X^0_{O_2} \frac{\dot{m}_{in}}{M_{in}} + E(\Delta\dot{m}_{O_2})_{NCA} \quad (14)$$

4. Results and Discussion

4.1 Burning behaviour

During the fire test, it was found that the cells did not burn after being subjected to incident heat fluxes of 10 and 15 kW m^{-2} for 1 hour. For the cell exposed to incident heat flux of 15 kW m^{-2}, only the pressure valve opened at 2190s into the test. The cells exposed to incident heat fluxes of 20 and 30 kW m^{-2} experienced only deflagration whereas the cells exposed to incident heat flux of 35, 40, 50 and 65 kW m^{-2} exhibited both mild burning deflagration. For comparison of this change, Figure 2 shows the fire behaviour of the cells exposed to 30, 35 and 65 kW m^{-2}.

As shown in Fig.2 (a), for the cell exposed to 30 kW m^{-2} incident heat flux, it experienced three stages during the test. Firstly, the cell was heated and started to release gas from 625 s, accompanied by opening of the pressure valve, which was marked by a distinctive sound. During the next 409s, the gas continued to release from the thermal reactions within the cell. Then at 1034s, noticeable spark was observed from the cell and simultaneously ignited the venting gas surrounding the cell and resulted in a deflagration, which was accompanied by jet flames emerging from the safety valve. Because there are three venting holes at the connection between the positive tab and the cell, the jets of the flame formed a lotus-like flame structure with three flames initially, they merged to two-flames vertically and eventually one-flame. After burning for 25 s, the fire extinguished.

For the cells exposed to incident heat fluxes of 35 and 65 kW m^{-2}, two burning processes occurred. As shown in Fig.2 (b) and (c), the burning behaviour can be classified into six stages. During the first stage, the venting gas was released through the opening of the pressure valve at 473 and 249 s, for cells exposed to incident heat fluxes of 35 and 65 kW m^{-2}, respectively. Immediately following the opening of the pressure valve, a small bright flame appeared near the heater and on the top of the cell, as shown in the first stage in Fig. 2 (b) and (c). Then the vented gas which gathered above the cell was ignited in half second. After the burst of the fire, the lotus-like jet fire with three flames was vertically formed and lasted 17 and 25 seconds, for cells under heat fluxes of 35 and 65 kW m^{-2}, respectively. After the flame faded, the cells were still heated. Then the cells went to deflagration after another 232 and 143 seconds, respectively. As shown in the stage IV in Fig. 2 (b) and (c), the vented gas surrounded the cell was ignited by the spark ejected from the cell, rather than the heater. This explosive burning is similar to that observed in stage II in Fig.2 (a), and after that, the following stages V and VI were also similar to the last two stages shown in Fig. 2 (a).

When the vented gas deflagrated, the cells burned intensely and ejected smoke with high pressure. Enormous particles with high temperature were also ejected. Especially for the cells exposed to incident heat fluxes of 50 and 65 kW m^{-2}, the high pressure even broke the steel can of the cells. Several rupture and small holes were found at the body of these cells.

Table 1 summarizes the parameters, which characterize the burning behaviour of the cells in these tests. It can be found that with the increase of the incident heat flux, the time to the opening of the pressure valve and the time to the explosive burning both decreased. Higher incident heat flux contributed to faster temperature increase, thus the consequent thermal reactions within the cell may occur more quickly. This means more gas generated and faster pressure increase for cells under higher incident heat flux.

4.2 Temperature variations

Figure 3 shows the temperature variations of the cell surface and the flame (left Y coordinate axis), and the temperature increase rates of the cell surface (right Y coordinate axis) during tests for cells exposed to various incident heat fluxes. The detailed critical temperature values were summarized in Table 1. The pressure valve of the cell exposed to incident heat flux of 10 kW m^{-2} did not open during the test, and it was found to have the highest surface temperature of 102 ºC.

The pressure valve opened at 2190s for the cell exposed to incident heat flux of 15 kW m^{-2}, when the surface temperature of the cell increased to 132 ºC. During the test, the cell showed highest surface temperature of 139ºC. The pressure valve started to open when the surface temperature increased to 133~165 ºC for cells exposed to incident heat fluxes of 20~65 kW m^{-2}. Generally, the increase rate of the cell surface temperature decrease with the pressure valve opening because of the Joule-Thomson expansion. It can also be seen that the surface temperature for the pressure valve opening increases with the increasing incident heat flux. The reason may lie in two aspects: 1) the higher incident heat flux would also lead to higher ambient

temperature surrounding the cell, resulting in the decrease of the heat loss term as in Eq. (5); 2) under higher incident heat flux, the cell temperature increased more quickly but more time was required for the pressure to build up and trigger the opening of the pressure valve.

After the surface temperature reached to 199, 203, 208, 213, 215 and 220 ºC, the deflagration happened to the cells exposed to incident heat flux of 20~65 kW m^{-2}. Although the induction leading to the deflagration was different in each case, the deflagration always occurred when the surface temperatures were close to 200 ºC. Generally, for all the tested cells, it was found that the temperature increase rates were over than 0.5 ºC s^{-1} just before the deflagration happened.

For all the cells, the peak temperature of the cell surface and the flame appeared at the time of deflagration. When the heat flux was higher than 40 kW m^{-2}, the steel can of the cells deformed and ruptured owing to the sharp increase in the pressure within the cell. Hence the thermocouple fixed to the surface of the cell came off due to the strain. As a result, the peak temperatures of the cell surface were only 326 and 407 ºC, for cells under heat flux of 50 and 65 kW m^{-2}, respectively. Whereas the cell surface could reach to higher than 800 ºC in the cases of heat flux of lower than 40 kW m^{-2}. Similarly, when the incident heat flux increased up to 40 kW m^{-2}, the deflagration became more intense and the thermocouples above the cell were blown away from the original location. Then the thermocouples were not exactly within the flame envelope, thus the peak temperatures of the flame for these cases were lower than 1000 ºC. However, for cells under incident heat flux of less than 40 kW m^{-2}, the peak temperatures of the flame were higher than 1000 ºC. It should be noted that the response time of the thermocouples employed in this work was 1 s and might not be sufficiently fast to record the temperature variation at the time of deflagration. For all the cells, their maximum temperature increase rates in each test were all over than 50 ºC s^{-1}. The maximum temperature increase rate detected during deflagration was 196 ºC s^{-1}, which occurred to the cell tested under 40 kW m^{-2}. These

values are much higher than the maximum acceptable self-heating rate (1.7 ºC s^{-1}) for a controlled engineering practice for safety design [27].

4.3 Thermal reactions

It is well known that the Li-ion cells develop TR under high temperatures. The basic cause to TR is thermal reactions among the cell materials, which increase heat and pressure within the cell. To investigate the contribution and sequence of thermal reactions triggering the fire, the thermal behaviour of the cell materials were analysed. Figure 4 shows the heat flow of different cell materials obtained by DSC tests.

Given that the pressure valves of the cell opened when the cell surface temperature was between 132~167ºC, heat generated around this temperature range may be the main cause to the open. As shown in Fig.4, when the temperature was below 170 ºC, the separator and the lithiated graphite in contact with electrolyte both showed variation on the heat flow. As shown in Fig. 4 (a), the separator showed two heat absorption processes. It melted partly within the temperature range of 122~162 ºC and then kept stable until 350 ºC. With the increase of the temperature, the separator melted completely from 350 ºC to 500 ºC. The first melting process led to a slight short circuit between the positive and negative electrodes. Consequently, the joule heat accompanied with the short circuit could be one of the contribution of the heat generation within the cell from 120 to 165 ºC. Moreover, the first weak exothermic peak occurred as in Fig. 4 (c), indicating that the SEI on the surface of the lithiated graphite decomposed and generated heat, and the following reaction took place:

$$(CH_2OCO_2Li)_2 \rightarrow Li_2CO_3 + C_2H_4 + CO_2 + \frac{1}{2}O_2 \quad (15)$$

The electrolyte can also decompose and release heat and gas during this temperature range, as suggested in previous research [28]. The following reactions may occur:

$$LiPF_6 \rightarrow LiF + PF_5 \quad (16)$$

$$PF_5 + H_2O \rightarrow PF_3O + 2HF \quad (17)$$

$$\begin{aligned} &ROCO_2R + PF_5 \rightarrow \text{-}CH_2CH_2OCO_2\text{-}CH_2CH_2OCO_2PF_5 \\ &\rightarrow \text{Oligo-ether Carbonates} \rightarrow PEO + nCO_2 \end{aligned} \quad (18)$$

$$C_2H_5OCO_2C_2H_5 + PF_5 \rightarrow C_2H_5OCO_2PF_4 + HF + C_2H_4 \quad (19)$$

$$C_2H_5OCO_2PF_4 + HF \rightarrow PF_4OH + C_2H_5F + CO_2 \quad (20)$$

Meanwhile, the boiling points of the solvents are 91, 110 and 126 ºC for DMC, EMC and DEC, respectively. Solvents would become to vapour and increase the pressure within the cell. Therefore, the short circuit induced by partly melting of separator, the decomposition of SEI and electrolyte, and the vapourization of solvents mainly contribute to the increased heat and pressure within the cell. Consequently, the elevated pressure within the cell gave rise to the open of the safety valve.

During the temperature range of 165~185 ºC, Fig. 4 (a), (b) and (c) all showed slight variations on heat flows. Few heat was released and thus the cells did not present remarkable fire and thermal behaviour during this range. When the temperature was higher than 185 ºC, as shown in Fig. 4 (b), the charged cathode in the present of electrolyte started to release heat significantly. Then the heat flow reached three exothermic peaks at 215, 239 and 414 ºC, respectively. When the temperature is lower than 500 ºC, the cathode decomposition is accompanied with oxygen release and correlated to two structural changes, from the layered (space group $R\bar{3}m$) to the disordered spinel ($Fd\bar{3}m$) and then to the rock-salt ($Fm\bar{3}m$) phase [29]:

$$Li_x(Ni_{0.8}Co_{0.15}Al_{0.05})O_2(R\bar{3}m) \rightarrow \frac{1+x}{3}[Li_{\frac{3x}{1+x}}(Ni_{0.8}Co_{0.15}Al_{0.05})_{\frac{3}{1+x}}O_4](Fd\bar{3}m) + \frac{1-2x}{3}O_2 \quad (21)$$

$$Li_x(Ni_{0.8}Co_{0.15}Al_{0.05})O_{\frac{4(1+x)}{3}}(Fd\bar{3}m) \rightarrow Li_x(Ni_{0.8}Co_{0.15}Al_{0.05})O_{1+x}(Fm\bar{3}m) + \frac{1+x}{6}O_2 \quad (22)$$

Meanwhile, the solvents burned by the released oxygen, with large amount of heat and gas

generation:

$$O_2 + ROCOOR \rightarrow CO + CO_2 + H_2O \quad (23)$$

By comparing with results summarized in Table 1, it can be found that the deflagration happened to the cells when their surface temperature were around 199~225 ºC. This indicates that the deflagration was mainly assigned to the fast exothermic process attributed to the cathode decomposition. In addition, as shown in Fig. 4 (c), the anode present in the electrolyte released heat from 200 ºC, and then showed thermal peaks at temperatures of 259 and 300 ºC. This implies that the anode relevant thermal reactions also contributed to the deflagration. These reactions are owing to the active lithium in the anode, which can react with water, HF, solvents and binder as following:

$$Li + H_2O \rightarrow Li_2O + H_2 \quad (24)$$

$$Li + HF \rightarrow LiF + H_2 \quad (25)$$

$$Li + C_3H_4O_3 \rightarrow Li_2CO_3 + C_2H_4 \quad (26)$$

$$Li + C_3H_6O_3 \rightarrow Li_2CO_3 + C_2H_6 \quad (27)$$

$$\text{-}CH_2CF_2\text{-} + Li \rightarrow \text{-}CH{=}CF\text{-} + LiF + H_2 \quad (28)$$

Considering the lower flammability limit (LFL) of CO, H_2, C_2H_4 or C_2H_6 is 12.5%, 4%, 3.1% or 3%, the deflagration observed in the tests might be arising from these flammable and explosive gas.

Figure 5 shows the XRD pattern of the electrodes before and after the fire test for the cells. As presented in Fig. 5 (a), a delithiated phase of LNCA and lithiated phase of Li_xC_6, were found, before the fire test for the 100% SOC cell. After the fire tests, the electrodes and current collectors in the cell became fragile and could not be separated easily. Thus the XRD pattern of the electrodes after the fire test showed the mixture of the electrodes. Figure 5 (b) shows that the XRD patterns of the electrodes obtained from cells exposed to different thermal radiations were

similar. All of them show evident phases of C and Ni, which should be the products of the graphite and LNCA electrodes, respectively. As shown in Fig. 3, the surface temperature of the cells during the tests even reached to over 800 ^{o}C. Given the appearance of the Ni phase, it can be confirmed the cathode continued to decompose when the temperature is extremely high. The rock-salt phase cathode might to decompose to metal oxide and even metal as the following:

$$\mathrm{Li}_x(\mathrm{Ni}_{0.8}\mathrm{Co}_{0.15}\mathrm{Al}_{0.05})\mathrm{O}_{1+x} \rightarrow \mathrm{NiO} + a\mathrm{Li}_2\mathrm{O} + \mathrm{Li}_{x-2a}\mathrm{M}_y\mathrm{O}_z + b\mathrm{O}_2 \quad (29)$$

$$\mathrm{NiO} \rightarrow \mathrm{Ni} + \frac{1}{2}\mathrm{O}_2 \quad (30)$$

For determining the details and differences in these XRD patterns, the enlarged patterns for cases of 30, 40 and 50 kW m^{-2} were shown in Fig. 5 (a) ~ (c). For the case of 65 kW m^{-2}, the deflagration was too intense and a large amount of the materials was blew off. As a result, the electrodes after burning was not tested for this case. As shown in Fig. 5, all of the patterns show clear phases of Li_2CO_3, LiF and Li_2O, which are products from reactions described as Eq. (15) to (29). No obvious cobalt and aluminum compounds were found in the XRD patterns. This should be arising from the little content of them in the initial cathode material. Moreover, few NiO phase was found for the cell exposed to 30 kW m^{-2}, but was found clearly in cases of 40 and 50 kW m^{-2}. This might be arising from the larger internal temperature discrepancy exists in the cells, with the increase of the external thermal radiation. Correspondingly, the temperature of the cell close to the thermal radiator increased quickly while the temperature of the cell far from the thermal radiator increased not so quickly. As a result, some cathode underwent partial decomposition rather than complete decomposition, and correspondingly with products of NiO.

4.4 Production of COx and weight variation

Another important factor of Li-ion cell fire is the toxic gas released during the burning. The production of toxic gas could come from thermal decomposition, liquid evapouration and the chemical reaction between the cell compounds [30]. In this study, the gas we focused on the CO_x (CO and CO_2), which is related to the assessment of the combustion overall

efficiency and the value of heat release rate (HRR). The production of CO_x during the burning test under different incident heat flux is shown in Fig. 6. It can be found that the generated CO and CO_2 during the burning process increased with the increasing thermal radiation. In particular, the increase margin of CO is much larger than that of CO_2. When the thermal radiation is 20 and 30 kW m^{-2}, the generated CO is quite small, which indicates that products of the incomplete combustion are rather small. As the increase of the thermal radiation, the products of the incomplete combustion increased evidently in the venting gas. As shown in Fig.6 (c)~(f), for cells underwent one mild burning and one deflagration, little CO was found for the first burning whereas CO_2 was found for both two burning processes. As the temperature of the cell during the first burning process is lower than 200 ºC, the amout of the gas generated in the cell from reactions as Eqs. (15)-(20) and the solvents vapour is not large. Few incomplete combustion occurs during the first burning process. However, a large amount of gas was generated from reactions as described in Eq. (21)-(30). It led to a large amount of ejecta in a short time. A rather low combustion efficiency was formed and more CO was generated. Such phenomena can also be further confirmed by Fig. 7, where a dramatic mass loss can be found due to the deflagration.

Figure 7 shows the mass loss of cells exposed to various incident heat fluxes. The overall mass loss ratio of a cell during test is 37.5, 38.6, 41.9, 42.3, 48.5 or 54.7%, for cell exposed to incident heat flux of 20, 30, 35, 40, 50 or 65 kW m^{-2}, respectively. The primary differences on the mass loss for different cells lie in the deflagration process. The mass loss with the deflagration was dependent on the incident heat flux. The mass loss companied with the open and the possible following ignition showed no significant differences among tested cells. For cells exposed to different incident heat flux, they showed about 5.9~9.3% mass loss before deflagration. Figure 6 (a)~(b) show no obvious peak of CO or CO_2 with the open, this implies that the mass loss with the open is mainly contributed by vapourization of solvents. One thing

should be noted is the transient mass loss at the instant of the open is -0.36, -0.55, -0.68, -0.69, -0.89 or -1.1g, for cell exposed to incident heat flux of 20, 30, 35, 40, 50 or 65 kW m^{-2}, respectively. The difference among these values is believed as the main contribution to the fire occurs whether or not with the open. If the vapour is emitted with higher quantity, the concentration of the vapour in the air might be higher than its LFL. In consequence, the vapour is ignited by the heater. Otherwise, the ignition will not occur.

4.5 Energy balance of the cell and HRR of the combustion

Following the analysis in section 3, the energy balance equation for the cell is mainly controlled by the energy source and loss. The two parts of energy variation counterbalance each other, which lead to diversified responses of cells exposed to different incident heat flux. Generally, the behaviour of the tested cells and their energy balance under over-heating can be summarized as going through the following phases:

Preheating: T$\leqslant$100 ^{o}C, the pressure valve does not open. The temperature elevates mainly because of the heater. If the heat obtained from the heater, Q_{heater}, is not high enough, and keep balance with the Q_{conv} and $Q_{rad,cell}$, the temperature of the cell will not continue to increase. Otherwise, the temperature of the cell will reach to higher level, and the behaviour of the cell expands into next phase.

From onset of thermal reactions to open of cell: 100 ^{o}C<T<165 ^{o}C, pressure valve opens following with this phase. During this phase, the liquid electrolyte, SEI and separator start to cause heat generation, which can be characterized by Q_{rec}. Meanwhile, a part of electrical energy converts into heat with the partly melting of separator, shown as Q_{elec}. The heat within the cell and from the heater co-work and cannot be negated by the heat loss Q_{conv} and $Q_{rad,cell}$. Consequently, the improved temperature and pressure in the cell lead to opening of the pressure valve.

Venting or mild ignition: 130 ^{o}C<T<170 ^{o}C. The flammable vapour is emitted from the

cell to the surroundings and takes away some part of energy (Q_{eject}). The flammable vapour-air mixture is formed and could be ignited by the heater, if the concentration of the vapour in air is higher than its LFL. For cells exposed to lower incident heat flux, the vapour released might not be sufficient to be ignited. Then the venting continues without burning.

Venting fading or flame extinguishment: 160 °C≤T≤180 °C. From the outside, the cell is heated by the heater, as well as the radiation of possible flame. From the inside, the cell is heated by the thermal reactions. Whereas, the vapour is consumed with the burning process or venting, concurrently the activity of thermal reactions decreases, and hence the Q_{rec} becomes smaller. The heat loss still consists of Q_{eject}, Q_{conv} and $Q_{rad,cell}$. In consequence, the venting or flame mitigates. Once the vapour concentration is lower than its LFL, the flame extinguish.

Onset of catastrophic heat generation reactions: 180 °C≤T≤225 °C, presage of deflagration. When the temperature of the cell reached the onset temperature of the cathode decomposition and the anode relevant reactions, the exothermic reactions generated plentiful heat and gas, especially O_2 and flammable and explosive gas. Before the explosive gas emitting to the surroundings, it mixes with O_2 and possible air, and is ignited immediately when its concentration is over than the LFL, or LEL. The Q_{rec} is a dominant heat source in this phase.

Deflagration and following fire: 195 °C <T. As forerunner of the deflagration, sparks always are found spilling from the cell, not the surroundings. Instantaneously, the vapour within and above the cell is ignited and the deflagration appears. The sharp rise in temperature leads to totally melting of separator, then some electrical energy converts into heat (Q_{elec}). The cell also gets heat from the radiation of the flame and heater (Q_{ext}). Meantime, energy is leaving owing to the massive ejecta, convection and radiation, shown as Q_{eject}, Q_{conv} and $Q_{rad,cell}$. Whereas the energy loss is far less than the energy source, the temperature of the cell increases to extreme high level (>800 °C). Owing to the sustained production of flammable

gas, the fire continues after the deflagration.

Extinguish and cooling: with the consumption of gas for deflagration, and no more gas is generated by thermal reactions, the fire is hard to continue. The heat source only includes $Q_{rad,heater}$, then the cell starts to cool down and eventually the temperature of the cell keeps in a constant, which is the combined effect of the $Q_{rad,heater}$, Q_{conv} and $Q_{rad,cell}$.

After understanding the energy balance, fire and deflagration behaviour of cells under over-heating, it is necessary to characterize the hazards of fire and deflagration. As the common indicator of fire hazard, HRR is calculated as methods described above. Figure 8 shows the HRR variation versus time for the cells exposed to different heat fluxes. The number of HRR peaks were similar to that of the number of burning processes. Corresponding to the time of the various cell behaviours, the first weak HRR peak shown in Fig. 9 (d)-(f) and the sharp increased HRR peak shown in Fig. 9 (a)-(f) are arising from the mild fire and the deflagration, respectively. The effect of the venting without fire is trivial for cells under 20 and 30 kW m^{-2}. The values of HRR peak corresponding to deflagration for cells under 20, 30, 35, 40, 50 and 65 kW m^{-2} are 8.2±0.05, 8.9±0.05, 9.4±0.05, 9.7±0.05, 10.4±0.05 and 11.8±0.05kW, respectively. It can also be found that the value of the main HRR peak increases with the increasing incident heat flux. In addition, the time reaching the main HRR peak reduced from 750s to 420s when the incident heat flux increased from 35 to 65 kW m^{-2}. Such phenomena indicate the reactions inside of cell will be quicker and stronger when the cell is exposed to a larger incident heat flux. As a result, more heat will be released. This conclusion can also be confirmed by the changing trend of the mass loss. Based on the HRR curves, the heat generation of the combustion for cells exposed to 20, 30, 35, 40, 50 and 65 kW m^{-2} are133.9±1.5, 138.5±1.5, 146.1±1.5, 147.3±1.5, 153.5±1.5 and 163.1±1.5 kJ, respectively.

Comparing to the discrepancy in mass loss measured in different tests, it can be found

the heat generation shows less discrepancy for cells under different heat fluxes. Although cells under 65 kW m^{-2} show significant mass loss, the combustion efficiency is not high as the cells under 35 kW m^{-2}. Moreover, the combustion heat obtained in this study is much greater than the heat released during TR for the same kind of LNCA cell in Ref. [31], which is determined as 29.5± 1.8kJ. The significant differences lie in two aspects: (1) the reference did not account for the heat of the fire and deflagration. The released heat is determined as the temperature rise multiplied by the specific heat capacity and the mass of the cell. However, the huge combustion heat of the flammable vapour was not included. (2) the thermal ramp in Ref. [31] is 0.5 $^{o}C\ min^{-1}$, which is quite smaller than the heating rates employed in the tests of this study. Considering the power of the heating source play important role on the variation of HRR and quantity of released heat, it is reasonable that the values obtained in this study are much higher.

5. Conclusions

The study examined the burning behaviour and hazards of LNCA cells using the cone calorimeter under different incident heat fluxes. The behaviour of the cell under over-heating was related to the incident heat flux. When the incident heat flux was 10 or 15 kW m^{-2}, no fire was observed. When the cell was exposed to the incident heat fluxes of 20 or 30 kW m^{-2}, one deflagration was observed. When the incident heat flux increased to 35 kW m^{-2}, mild burning was followed by turbulent deflagration. With the over-heating by the heater, the temperature of the cells increased, the separator, electrolyte and SEI caused heat and gas release, which leads to the opening of the pressure valve. The flammable vapour was emitted from the cell to the surroundings, and prone to ignition by the heater if the concentration of the vapour in air within the flammability range. After the opening of the pressure valve, as the vapour is consumed with the burning process, the flame mitigates and would disappear if the new generated gas is not abundant to support the essential requirements of the burning. When the

temperature of the cell reached the onset temperature of the cathode decomposition, the fast exothermic process was activated. Reactions among cell materials generated explosive gas and oxygen. The mixture was then ignited immediately in the cell, when the concentration of the explosive gas was within the flammability range.

For all tested cells exposed to different incident heat fluxes, the discrepancy on the extreme temperature of the cell and the burning is small. All cells present the maximum temperature of the cell surface and the flame over than 800 and 1000 ^{o}C. Whereas the mass loss and HRR are higher when the cells are exposed under larger incident heat flux. Cells heated under 65 kW m^{-2} release as high as 163.1±1.5kJ and exhibit 54.7% mass loss during the fire and deflagration.

From the analysis in this work, the main hazard of the fire and deflagration is the huge heat released and extreme temperature, as well as the explosive gas which is also toxic. From the safety perspective, the following points need to be noted for application of the same kind of cells studied here:

(1) It is important to prevent the temperature of the cell increasing to over 100^{o}C, which is close to the onset range of the initial thermal reactions within the cell.

(2) If the temperature of the cell is already higher than 100^{o}C, effective cooling strategy should be employed to prevent the progress of the potential TR. Such cooling should be part of the BTMS.

(3) If the cell is already burning, reducing its temperature through cooling is essential and urgent for firefighting. If the initial fire could be put out, the hazard of the cell fire might be controlled in a more tolerable level. Otherwise, people should stay away from the cell or electronics, and leave them in an environment without combustibles.

(4) Even after the flame was quenched, the cell could might still undergo more severe

events, such as deflagration. Therefore, it is critical to employ sufficient fire-extinguishing agent to cool down the cell; and prevent the cell temperature to increase any further.

(5) Considering colossal amount of energy could be released in very short time due to cell deflagration, a potential TR of a single cell could lead to catastrophic event of a battery module or whole pack. To prevent the propagation of TR, interventions like cooling should be considered in BTMS.

The investigation of this study provides an insight of the fire and deflagration behaviour and hazards of LICs. Such results are useful for the safety assurance and fire protection design of battery system, such as the high temperature control, selection of appropriate fire-extinguishing agent.

Acknowledgments

This work is supported by the National Natural Science Foundation of China (No. 51604297), the European Commission's Marie Curie Action, the Key Research and Development Program of Shandong Province (2018GSF120011) and the Fundamental Research Funds for the Central Universities (No. 18CX07005A and No. 16CX02045A). Dr Ping is supported by the Incoming International Fellowship grant (No. 656582).

References

[1] X. Feng, J. Sun, M. Ouyang, F. Wang, X. He, L. Lu, H. Peng, Characterization of penetration induced thermal runaway propagation process within a large format lithium ion battery module, Journal of Power Sources, 275 (2015) 261-273.

[2] D.P. Finegan, M. Scheel, J.B. Robinson, B. Tjaden, I. Hunt, T.J. Mason, J. Millichamp, M. Di Michiel, G.J. Offer, G. Hinds, In-operando high-speed tomography of lithium-ion batteries during thermal runaway, Nature communications, 6 (2015) 6924.

[3] F. Larsson, S. Bertilsson, M. Furlani, I. Albinsson, B.-E. Mellander, Gas explosions and thermal runaways during external heating abuse of commercial lithium-ion graphite-LiCoO 2 cells at different

levels of ageing, Journal of Power Sources, 373 (2018) 220-231.
[4] Z. Chen, P.-C. Hsu, J. Lopez, Y. Li, J.W. To, N. Liu, C. Wang, S.C. Andrews, J. Liu, Y. Cui, Fast and reversible thermoresponsive polymer switching materials for safer batteries, Nature Energy, 1 (2016) 15009.
[5] L. Jiang, Q. Wang, J. Sun, Electrochemical performance and thermal stability analysis of LiNixCoyMnzO2 cathode based on a composite safety electrolyte, Journal of hazardous materials, 351 (2018) 260-269.
[6] Z. Chen, R. Xiong, J. Tian, X. Shang, J. Lu, Model-based fault diagnosis approach on external short circuit of lithium-ion battery used in electric vehicles, Applied energy, 184 (2016) 365-374.
[7] S. Wilke, B. Schweitzer, S. Khateeb, S. Al-Hallaj, Preventing thermal runaway propagation in lithium ion battery packs using a phase change composite material: An experimental study, Journal of Power Sources, 340 (2017) 51-59.
[8] https://www.ntsb.gov/news/press-releases/Pages/NR20180509.aspx.
[9] M.J. Loveridge, G. Remy, N. Kourra, R. Genieser, A. Barai, M.J. Lain, Y. Guo, M. Amor-Segan, M.A. Williams, T. Amietszajew, Looking Deeper into the Galaxy (Note 7), Batteries, 4 (2018) 3.
[10] S. Hwang, S.M. Kim, S.-M. Bak, B.-W. Cho, K.Y. Chung, J.Y. Lee, W. Chang, E.A. Stach, Investigating local degradation and thermal stability of charged nickel-based cathode materials through real-time electron microscopy, ACS applied materials & interfaces, 6 (2014) 15140-15147.
[11] A.W. Golubkov, S. Scheikl, R. Planteu, G. Voitic, H. Wiltsche, C. Stangl, G. Fauler, A. Thaler, V. Hacker, Thermal runaway of commercial 18650 Li-ion batteries with LFP and NCA cathodes–impact of state of charge and overcharge, RSC Advances, 5 (2015) 57171-57186.
[12] Y.-S. Duh, M.-T. Tsai, C.-S. Kao, Characterization on the thermal runaway of commercial 18650 lithium-ion batteries used in electric vehicle, Journal of Thermal Analysis and Calorimetry, 127 (2017) 983-993.
[13] M. Lammer, A. Königseder, V. Hacker, Holistic methodology for characterisation of the thermally induced failure of commercially available 18650 lithium ion cells, RSC Advances, 7 (2017) 24425-24429.
[14] W.-C. Chen, C.-M. Shu, Y.-W. Wang, Effects of thermal hazard on 18650 lithium-ion battery under different states of charge, Journal of Thermal Analysis and Calorimetry, 121 (2015) 525-531.
[15] S. Yayathi, W. Walker, D. Doughty, H. Ardebili, Energy distributions exhibited during thermal runaway of commercial lithium ion batteries used for human spaceflight applications, Journal of Power Sources, 329 (2016) 197-206.
[16] C. Y. Jhu, Y. W. Wang, C. M. Shu, J. C. Chang, H. C. Wu, Thermal explosion hazards on 18650 lithium ion batteries with a VSP2 adiabatic calorimeter, Journal of hazardous materials, 192 (2011) 99-107.
[17] S.J. Harris, A. Timmons, W.J. Pitz, A combustion chemistry analysis of carbonate solvents used in Li-ion batteries, Journal of Power Sources, 193 (2009) 855-858.
[18] P.A. Glaude, W.J. Pitz, M.J. Thomson, Chemical kinetic modeling of dimethyl carbonate in an opposed-flow diffusion flame, Proceedings of the Combustion Institute, 30 (2005) 1111-1118.
[19] A. Palacios, M. Muñoz, R. Darbra, J. Casal, Thermal radiation from vertical jet fires, Fire safety journal, 51 (2012) 93-101.
[20] P.T. Coman, E.C. Darcy, C.T. Veje, R.E. White, Modelling Li-ion cell thermal runaway triggered by an internal short circuit device using an efficiency factor and Arrhenius formulations, Journal of The Electrochemical Society, 164 (2017) A587-A593.

[21] T.D. Hatchard, D. D. MacNei, D. A. Stevens, L. Christensen, J. R. Dahn. Importance of Heat Transfer by Radiation in Li-Ion Batteries during Thermal Abuse. Electrochemical and Solid-State Letters, 3 (2000) 305-308.
[22] W. Thornton, The Relation of Oxygen to the Heat of Combustion of Organic Compounds, Philosophical Magazine and J. of Science, (1917).
[23] C. Huggett, Estimation of the rate of heat release by means of oxygen Consumption, Journal of Fire and Flammability, 12 (1980) 61-65.
[24] M.L. Janssens, Measuring rate of heat release by oxygen consumption, Fire technology, 27 (1991) 234-249.
[25] L. Mu, R. Lin, R. Xu, L. Han, S. Xia, D. Sokaras, J. Steiner, T.-C. Weng, D. Nordlund, M.M. Doeff, Oxygen Release Induced Chemomechanical Breakdown of Layered Cathode Materials, Nano letters, (2018).
[26] O.S. Mendoza-Hernandez, H. Ishikawa, Y. Nishikawa, Y. Maruyama, M. Umeda, Cathode material comparison of thermal runaway behavior of Li-ion cells at different state of charges including over charge, Journal of Power Sources, 280 (2015) 499-504.
[27] J.-M. Hsu, M.-S. Su, C.-Y. Huang, Y.-S. Duh, Calorimetric studies and lessons on fires and explosions of a chemical plant producing CHP and DCPO, Journal of hazardous materials, 217 (2012) 19-28.
[28] P. Ping, Q. Wang, P. Huang, J. Sun, C. Chen, Thermal behaviour analysis of lithium-ion battery at elevated temperature using deconvolution method, Applied Energy, 129 (2014) 261-273.
[29] S.-M. Bak, K.-W. Nam, W. Chang, X. Yu, E. Hu, S. Hwang, E.A. Stach, K.-B. Kim, K.Y. Chung, X.-Q. Yang, Correlating Structural Changes and Gas Evolution during the Thermal Decomposition of Charged Li x Ni0. 8Co0. 15Al0. 05O2 Cathode Materials, Chemistry of Materials, 25 (2013) 337-351.
[30] P. Ribière, S. Grugeon, M. Morcrette, S. Boyanov, S. Laruelle, G. Marlair, Investigation on the fire-induced hazards of Li-ion battery cells by fire calorimetry, Energy & Environmental Science, 5 (2012) 5271-5280.
[31] M. Lammer, A. Königseder, V. Hacker, Characterisation of Heat and Gas Emissions in Thermally Induced Battery Failure on Commercially Available 18650 Li-Ion Cells, ECS Transactions, 80 (2017) 135-143.

Table 1 Summary of parameters for fire and deflagration of LNCA cells exposed to various incident heat fluxes.

Incident heat flux (kW m^{-2})	10	15	20	30	35	40	50	65
Number of times for ignition	0	0	1	1	2	2	2	2
Time to crack of pressure valve (s)	--	2190	1285	625	473	376	305	249
Time to Deflagration (s)	--	--	2325	1034	722	593	536	417
Duration for the 1^{st} burning (s)	--	--	--	--	17	15	16	25
Duration for the final burning (s)	--	--	20	25	18	16	13	10
Surface T just before the open of pressure valve (^oC)	--	132	133	139	156	158	160	165
Surface T just before Deflagration (^oC)	--	--	199	203	208	213	215	220
Mass loss (%)			37.5	38.6	41.9	42.3	48.5	54.7
Highest surface T (^oC)	102	139	829	869	838	876	326	407
Highest flame T (^oC)	--	--	1042	1037	1069	1043	928	747
Highest HRR (kW)	--	--	8.2±0.05	8.9±0.05	9.4±0.05	9.7±0.05	10.4±0.05	11.8±0.05
Heat release (kJ)	--	--	133.9±1.5	138.5±1.5	146.1±1.5	147.3±1.5	153.5±1.5	163.1±1.5

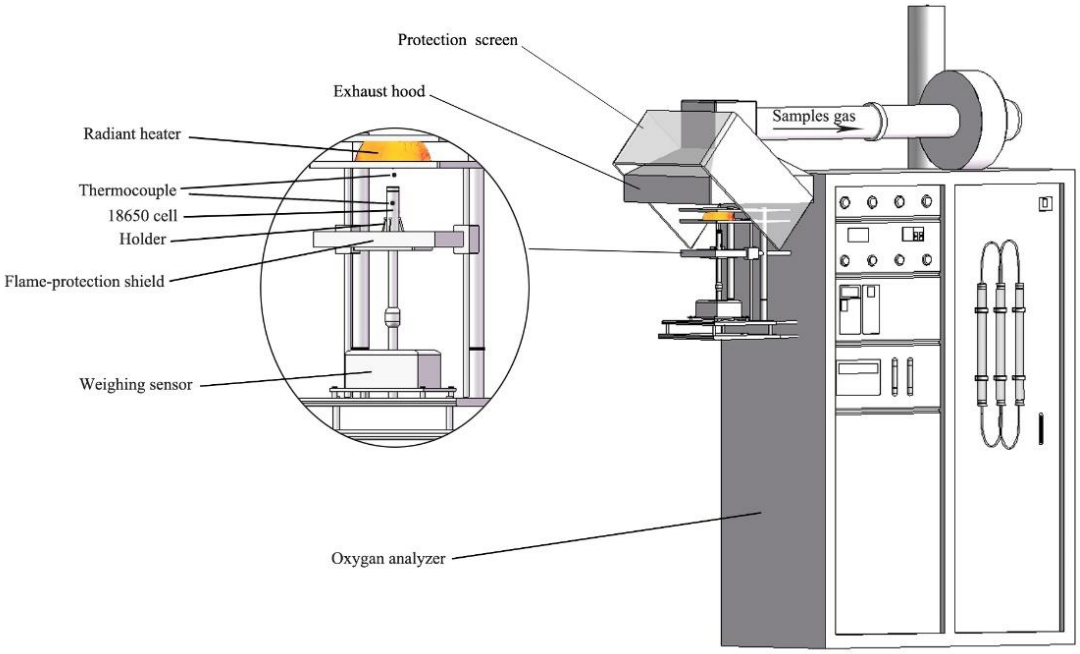

Fig.1 Schematic of fire test system.

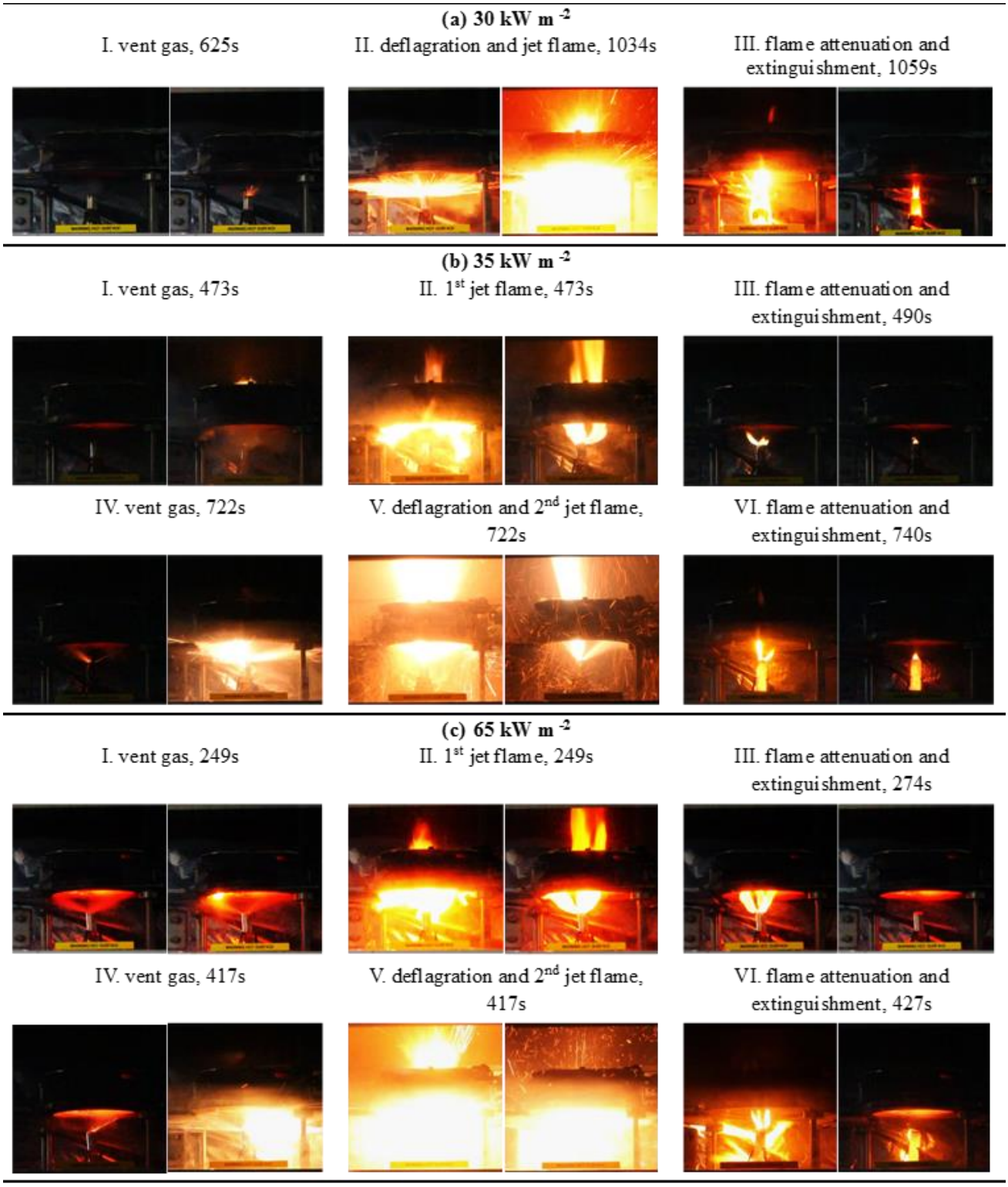

Fig.2 Fire behaviour of cells exposed to incident heat fluxes of (a) 30, (b)35, (c)65 kW m^{-2}.

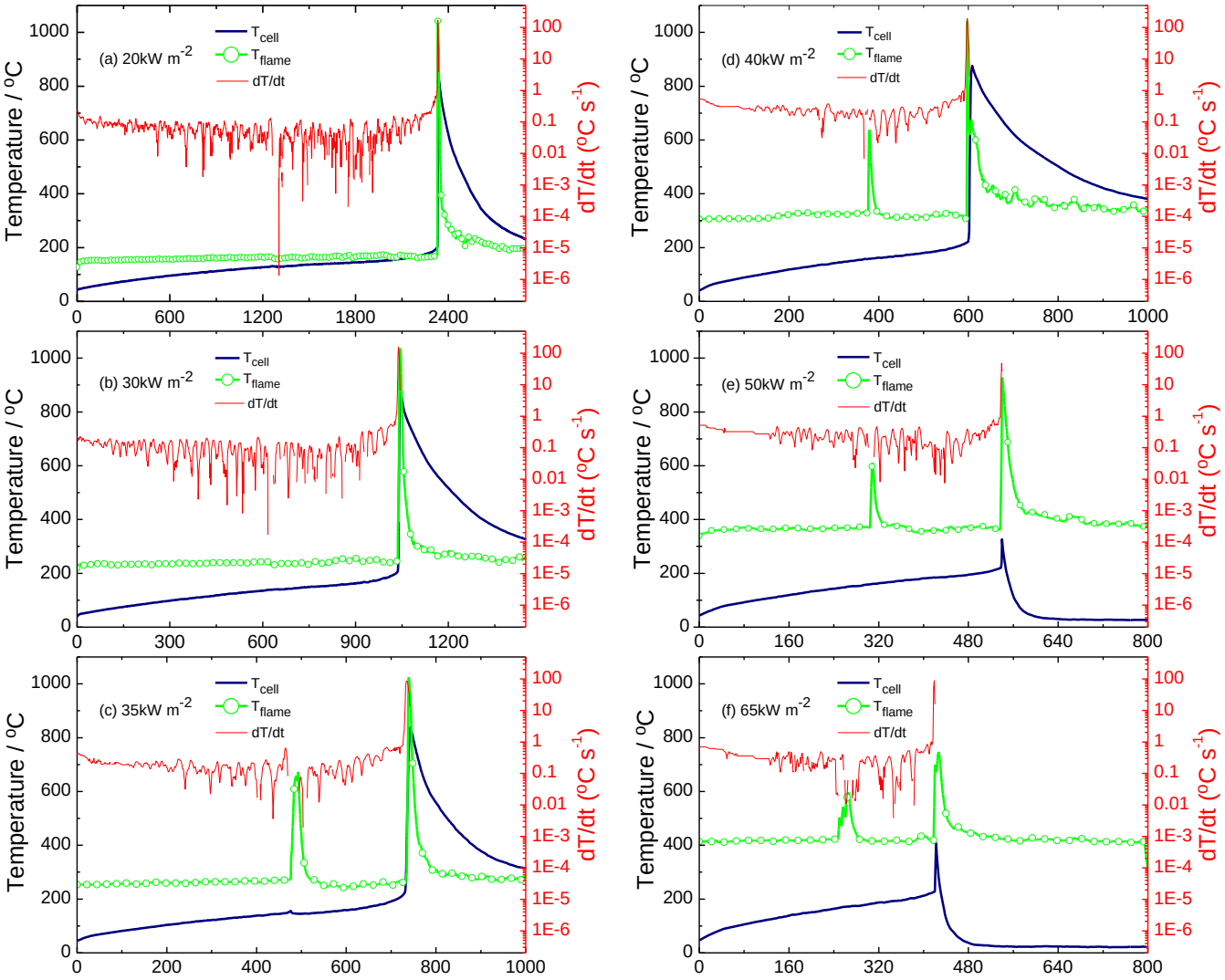

Fig.3 Temperature variations of cell surface and flame during fire test for cells exposed to incident heat fluxes of (a) 20, (b) 30, (c) 35, (d) 40, (e) 50 and (f) 65kW m^{-2}.

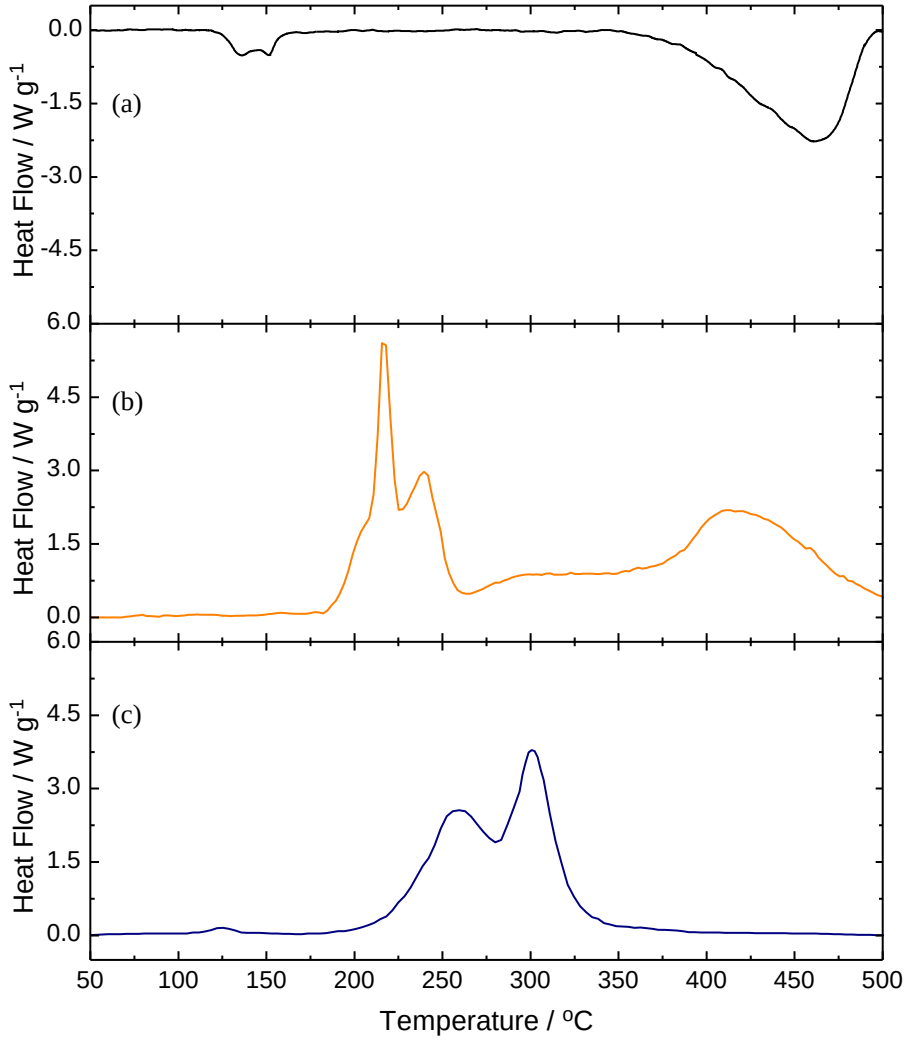

Fig.4 DSC heat flow curves of (a) separator, (b) cathode in the present of electrolyte and (c) anode in the present of electrolyte.

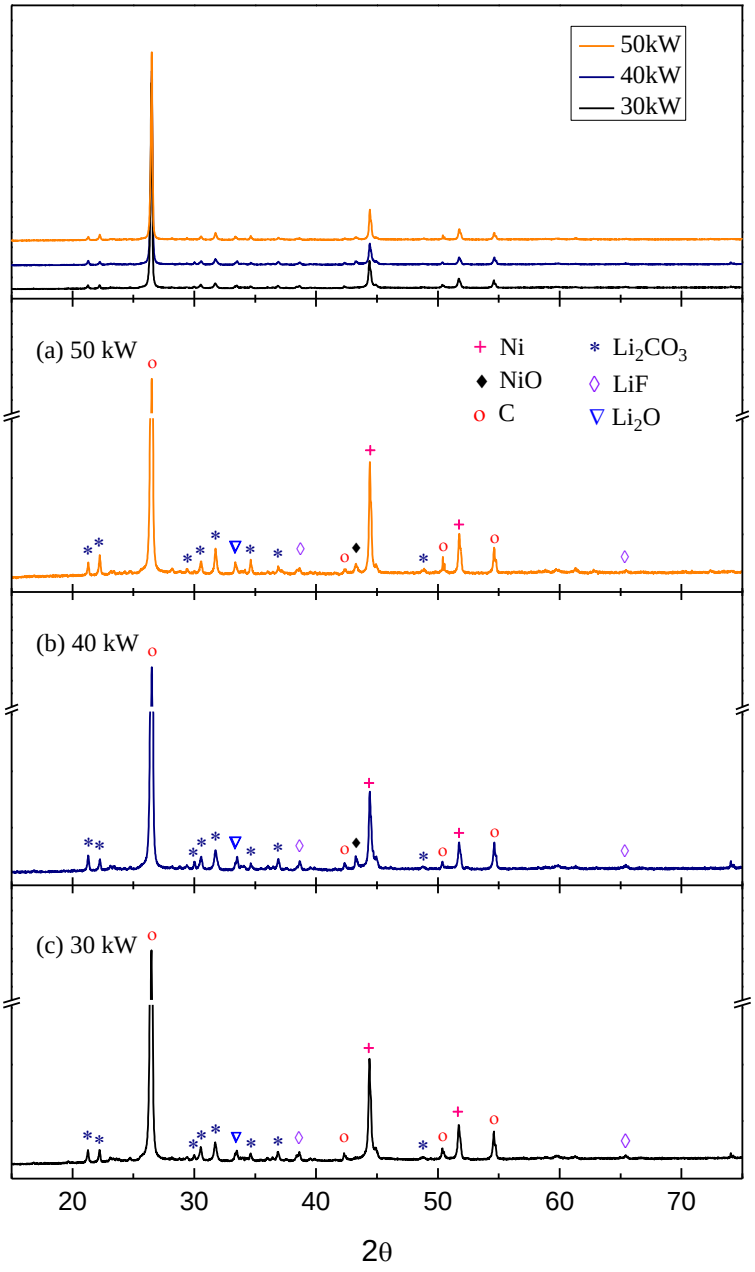

Fig.5 XRD patterns of electrodes after fire tests under (a) 50 kW, (b) 40 kW and (c) 30 kWm^{-2}.

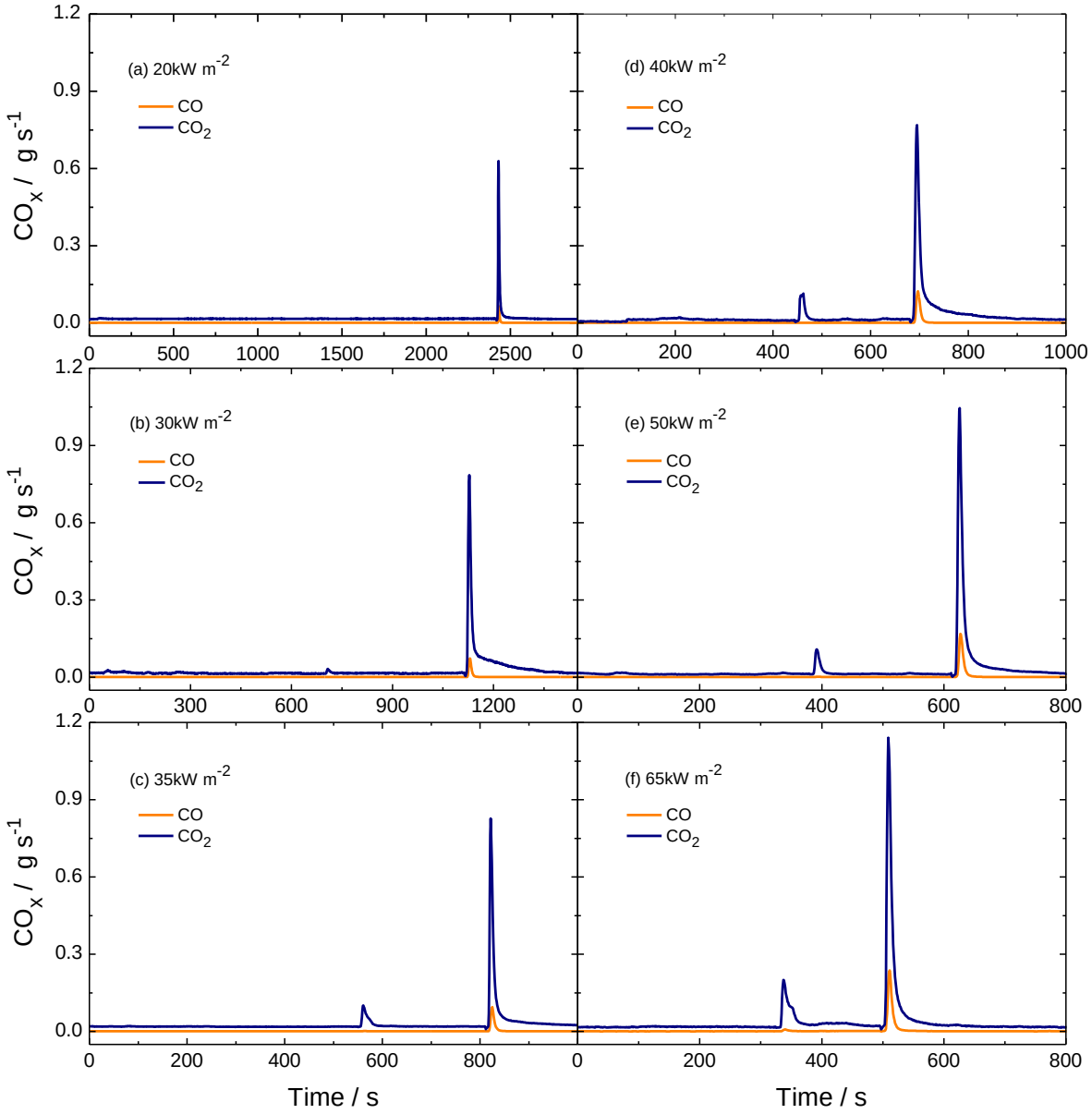

Fig.6 CO_2 and CO variations for cells exposed to incident heat fluxes of (a) 20, (b) 30, (c) 35, (d) 40, (e) 50 and (f) 65kW m^{-2}.

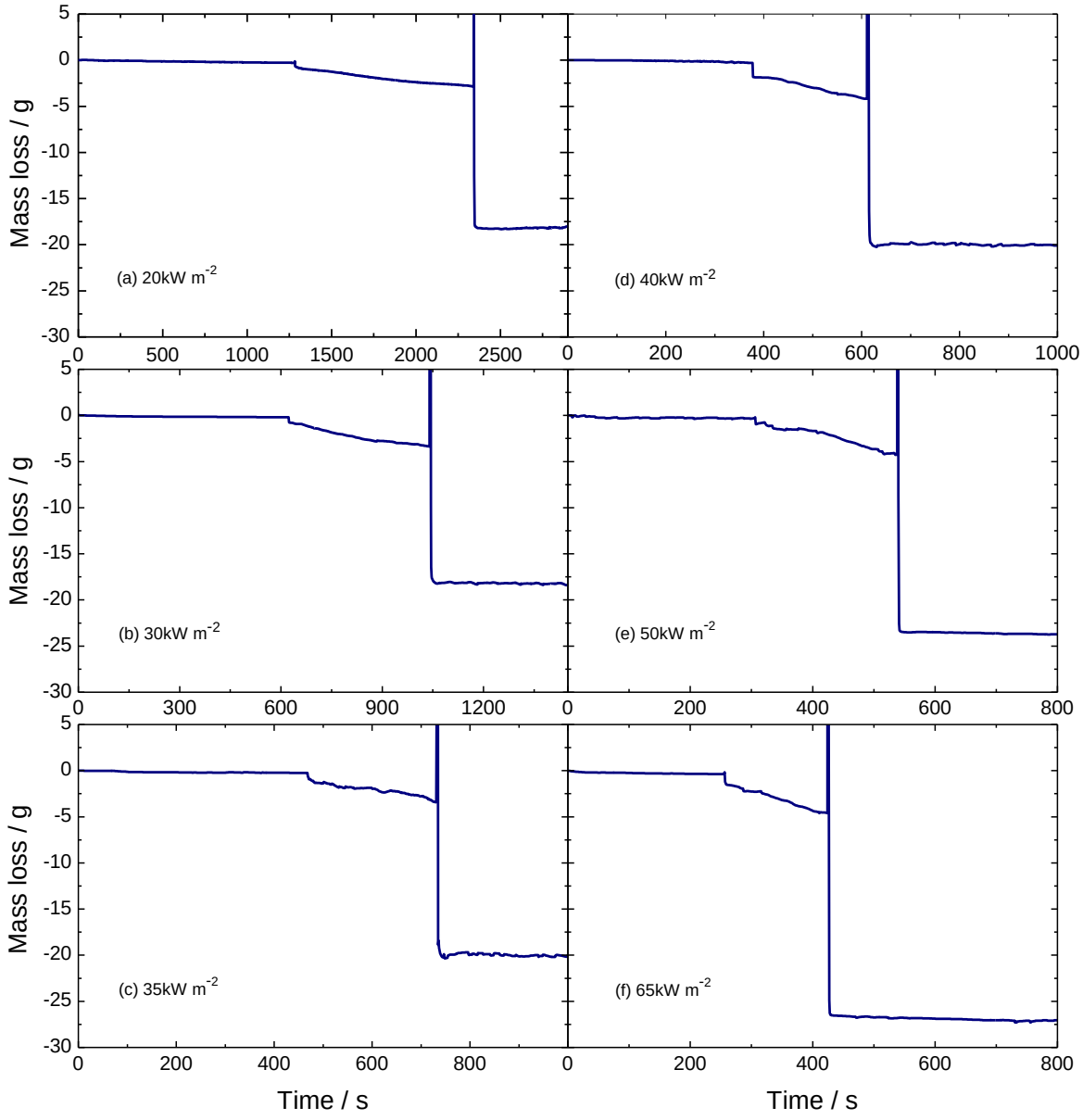

Fig.7 Mass loss of cells exposed to incident heat fluxes of (a) 20, (b) 30, (c) 35, (d) 40, (e) 50 and (f) 65kW m^{-2}.

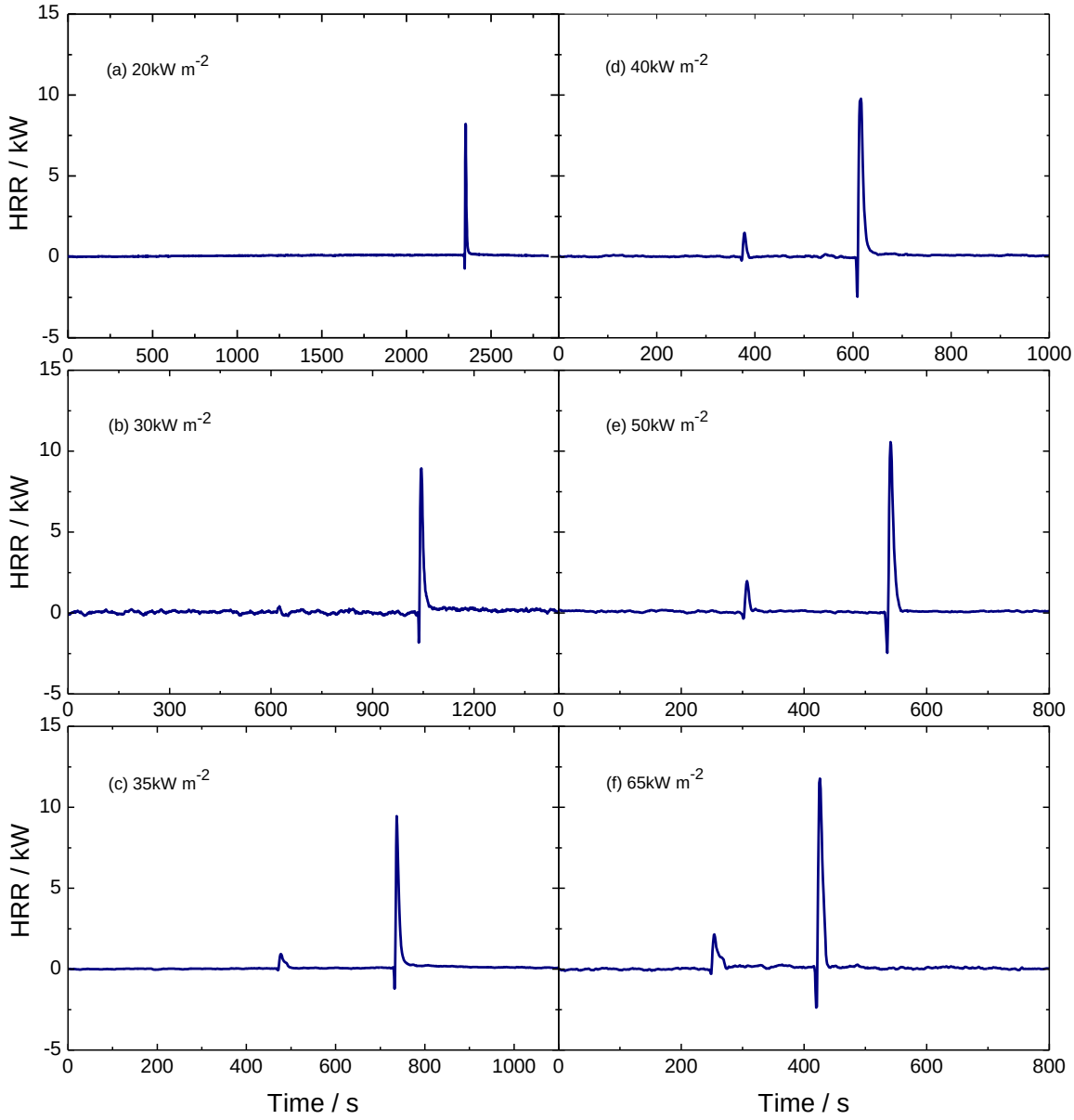

Fig.8 HRR variations for cells exposed to incident heat fluxes of (a) 20, (b) 30, (c) 35, (d) 40, (e) 50 and (f) 65kW m^{-2}.